

2D Layered Perovskites

Solution Processable Materials

The recent discovery that single-layer 2D perovskites can be prepared using solution processing techniques¹ has been followed by enormous research into optoelectronic applications of 2D perovskites including light emitting diodes (LEDs),² phototransistors,³ and solar cells.⁴

Tunable Emission Wavelength

Photoluminescent 2D perovskites have an emission wavelength that changes depending on the layer thickness and the choice of amine and halide. We offer an excellent portfolio of the most popular 2D perovskite compositions for photoluminescence based devices.

Improved Moisture Stability

Solar cells fabricated with 2D perovskites have improved stability in moist air compared to 3D perovskites.⁴



Formula	Cat. No.	Layer Thickness	$(\text{RNH}_3)_2(\text{MeNH}_2)_{n-1}\text{Pb}_n\text{X}_{3n+1}$		
			R	X	n
$(\text{BA})_2\text{PbI}_4$	910961	n=1	Bu	I	1
$(\text{BA})_2\text{PbBr}_4$	910953	n=1	Bu	Br	1
$(\text{PEA})_2\text{PbI}_4$	910937	n=1	PE	I	1
$(\text{PEA})_2\text{PbBr}_4$	910945	n=1	PE	Br	1
$(\text{BA})_2(\text{MA})\text{Pb}_2\text{I}_7$	912816	n=2	Bu	I	2
$(\text{BA})_2(\text{MA})_2\text{Pb}_3\text{I}_{10}$	912557	n=3	Bu	I	3
$(\text{BA})_2(\text{MA})_3\text{Pb}_4\text{I}_{13}$	914363	n=4	Bu	I	4
$(\text{BA})_2(\text{MA})_4\text{Pb}_5\text{I}_{16}$	912301	n=5	Bu	I	5

BA = n-butylammonium; PEA = 2-phenylethylammonium; MA = methylammonium, Bu=n-butyl, PE=2-phenylethyl

References:

- 1) Dou, L.; Wong, A. B.; Yu, Y.; Lai, M.; Kornienko, N.; Eaton, S. W.; Fu, A.; Bischak, C. G.; Ma, J.; Ding, T.; Ginsberg, N. S.; Wang, L.-W.; Alivisatos, A. P.; Yang, P. *Science* **2015**, *349*, 1518. DOI: 10.1126/science.aac7660
- 2) Yuan, M.; Quan, L. N.; Comin, R.; Walters, G.; Sabatini, R.; Voznyy, O.; Hoogland, S.; Zhao, Y.; Beauregard, E. M.; Kanjanaboos, P.; Lu, Z.; Kim, D. H.; Sargent, E. H. *Nat. Nanotechnol.* **2016**, *11*, 872. DOI: 10.1038/NNANO.2016.110
- 3) Shao, Y.; Liu, Y.; Chen, X.; Chen, C.; Sarpkaya, I.; Chen, Z.; Fang, Y.; Kong, J.; Watanabe, K.; Taniguchi, T.; Taylor, A.; Huang, J.; Xia, F. *Nano Lett.* **2017**, *17*, 7330. DOI: 10.1021/acs.nanolett.7b02980
- 4) Cao, D. H.; Stoumpos, C. C.; Farha, O. K.; Hupp, J. T.; Kanatzidis, M. G. *J. Am. Chem. Soc.* **2015**, *137*, 7843. DOI: 10.1021/jacs.5b03796

SigmaAldrich.com/perovskite

The Life Science business of Merck operates as MilliporeSigma in the U.S. and Canada.

© 2022 Merck KGaA, Darmstadt, Germany and/or its affiliates. All Rights Reserved. Merck, the vibrant M, and Sigma-Aldrich are trademarks of Merck KGaA, Darmstadt, Germany or its affiliates. All other trademarks are the property of their respective owners. Detailed information on trademarks is available via publicly accessible resources.

MK_AD9822EN 43729 09/2022

The Life Science business of Merck operates as MilliporeSigma in the U.S. and Canada.

Sigma-Aldrich[®]
Lab & Production Materials

TiO₂/FePS₃ S-Scheme Heterojunction for Greatly Raised Photocatalytic Hydrogen Evolution

Bingquan Xia, Bowen He, Jianjun Zhang, Laiquan Li, Yanzhao Zhang, Jianguo Yu, Jingrun Ran,* and Shi-Zhang Qiao*


The aggravating extreme climate changes and natural disasters stimulate the exploration of low-carbon/zero-carbon alternatives to traditional carbon-based fossil fuels. Solar-to-hydrogen (STH) transformation is considered as appealing route to convert renewable solar energy into carbon-free hydrogen. Restricted by the low efficiency and high cost of noble metal cocatalysts, high-performance and cost-effective photocatalysts are required to realize the realistic STH transformation. Herein, the 2D FePS₃ (FPS) nanosheets anchored with TiO₂ nanoparticles (TiO₂/FePS₃) are synthesized and tested for the photocatalytic hydrogen evolution reaction. With the integration of FPS, the photocatalytic H₂-evolution rate on TiO₂/FePS₃ is radically increased by ≈1686%, much faster than that of TiO₂ alone. The origin of the greatly raised activity is revealed by theoretical calculations and various advanced characterizations, such as transient-state photoluminescence spectroscopy/surface photovoltage spectroscopy, in situ atomic force microscopy combined with Kelvin probe force microscopy (AFM-KPFM), in situ X-ray photoelectron spectroscopy (XPS), and synchrotron-based X-ray absorption near edge structure. Especially, the in situ AFM-KPFM and in situ XPS together confirm the electron transport pathway in TiO₂/FePS₃ with light illumination, unveiling the efficient separation/transfer of charge carrier in TiO₂/FePS₃ step-scheme heterojunction. This work sheds light on designing and fabricating novel 2D material-based S-scheme heterojunctions in photocatalysis.

1. Introduction

Recently, extreme climate changes and natural disasters have alerted humans to the impact of global warming, which has

B. Xia, L. Li, Y. Zhang, J. Ran, S.-Z. Qiao
School of Chemical Engineering and Advanced Materials
The University of Adelaide
Adelaide, SA 5005, Australia
E-mail: jingrun.ran@adelaide.edu.au; s.qiao@adelaide.edu.au

B. He, J. Zhang, J. Yu
Laboratory of Solar Fuel
Faculty of Materials Science and Chemistry
China University of Geosciences
Wuhan 430074, P. R. China

 The ORCID identification number(s) for the author(s) of this article can be found under <https://doi.org/10.1002/aenm.202201449>.

© 2022 The Authors. Advanced Energy Materials published by Wiley-VCH GmbH. This is an open access article under the terms of the Creative Commons Attribution License, which permits use, distribution and reproduction in any medium, provided the original work is properly cited.

DOI: 10.1002/aenm.202201449

continually intensified and could be out of control. Therefore, it is urgent to greatly reduce the gigantic consumption of carbon-based fossil fuels,^[1,2] which emit substantial greenhouse gases and tremendously aggravate global warming. Furthermore, it is of great significance to realize carbon neutrality in human society via replacing fossil fuels with low-carbon/carbon-free alternatives. Thus, the conversion of renewable solar energy^[3–5] into clean and carbon-free hydrogen (H₂) fuel is highly attractive. Such a solar-to-H₂ (STH) conversion can be achieved utilizing photocatalytic H₂ evolution via water splitting,^[6–10] which is regarded as an alluring, environmentally benign and low-cost strategy. Hence, a highly active, robust, and affordable photocatalyst is the most sought after.^[11–13] The rational design and synthesis of such a photocatalyst require not only the emerging nanosized building blocks with desired features, but also efficient charge dissociation/transfer boosted by the strong built-in electric field in a favorable junction system.

In the past decades, 2D materials have demonstrated great capacity to achieve efficient and cost-effective photocatalysis for various reactions, due to their distinct physicochemical features.^[14–21] Recently, an emerging 2D material, FePS₃ (FPS),^[22–27] has displayed numerous attractive characteristics for catalysis: i) Ultrathin structure facilitating rapid bulk-to-surface electron-hole transport; ii) high specific surface area accelerating efficient adsorption/desorption of reactant and product, and benefiting the anchoring of other nanobuilding blocks; iii) exposed under-coordinated edge atoms serving as active sites to advance the reactions; iv) thickness-dependent electronic band structure promoting the regulation of light absorption and redox abilities of charge carriers; v) p-type semiconductor nature favoring the construction of certain junction system with a strong built-in electric field. Albeit the above alluring advantages,^[28–30] only a few works reported the application of FPS in photocatalysis. For instance, FPS quantum sheets show the photocatalytic H₂-evolution rate of 290 μmol h⁻¹ g⁻¹ in 10% triethanolamine aqueous solution under xenon light illumination.^[28] Porous FPS nanosheets exhibit the photocatalytic H₂-evolution activity of 305.6 μmol h⁻¹ g⁻¹ in 10% triethylamine aqueous solution with xenon light irradiation.^[29] Nevertheless, to the best of our

knowledge, no work reports the utilization of FPS to construct heterojunctions in photocatalysis.

It is a great challenge to accurately regulate the charge dissociation/transfer to achieve high charge utilization efficiency and maintain the strong redox abilities of electrons and holes in semiconductor-based photocatalysts.^[31–34] Recently, the step-scheme (S-scheme) heterojunction has emerged as a very effective junction system with a strong built-in electric field, which simultaneously boosts the splitting of electron-hole pairs and retains their high redox capacities.^[35–41] The detailed differences in the S-scheme heterojunctions compared with type II heterojunctions or Z-scheme heterojunctions are summarized in Table S1, Supporting Information.^[35,42] Especially, the S-scheme junctions based on an n-p junction system have been rarely reported.^[43] Additionally, the direct visualization of the charge carrier transport pathway in the S-scheme junction is challenging, but interesting and important for understanding the in-depth mechanism in photocatalytic reactions.^[44,45] This will further guide the rational design and synthesis of an efficient junction system toward targeted photocatalytic reactions. Atomic force microscopy combined with in situ Kelvin probe force microscopy (AFM-KPFM) can be used to explore the charge transfer course in photocatalysts with light illumination.^[46–49] Therefore, it is particularly important to apply in situ AFM-KPFM to study the charge transfer pathway in the S-scheme junction based on an n-p semiconductor system.

Herein, 2D FPS nanosheets (NSs) were decorated with TiO₂ nanoparticles (NPs) to form the S-scheme heterojunction of FPS/TiO₂ possessing a strong internal electric field, which significantly raised the photocatalytic H₂-evolution rate compared with TiO₂ NPs alone. The as-synthesized FPS/TiO₂ exhibited the H₂ evolution rate of 99.5 μmol h⁻¹ g⁻¹, surpassing that of TiO₂ alone by ≈1686%. The origin of the tremendously increased rate was studied by a series of cutting-edge characterizations, for example, transient-state photoluminescence/surface photovoltage spectroscopy, in situ AFM-KPFM, in situ X-ray photoelectron spectroscopy (XPS) and synchrotron-based X-ray absorption near edge structure (XANES). Notably, in situ AFM-KPFM was carried out to visualize the photogenerated charge migration path and surface potential changes of the as-prepared TiO₂/FPS with light excitation. Additionally, ex situ XPS and theoretical calculations revealed the intimate electronic interaction between TiO₂ and FPS. These results demonstrate that TiO₂ NPs coupled with novel 2D FPS NSs can form the S-scheme heterojunction based on an n-p semiconductor system, which not only greatly advances the electron-hole separation/transport, but also reserves the electrons and holes with higher redox capabilities on the conduction band of FPS and the valence band of TiO₂, respectively. Therefore, the photocatalytic H₂ evolution rate of FPS/TiO₂ S-scheme heterojunction is significantly raised.

2. Results and Discussion

2.1. Crystal Structure, Morphology, and Elemental Composition of FPS and FPS/TiO₂

The flake-like bulk FPS was ground for 0.5 h and then added into ethanol for the subsequent sonication and centrifuge treatment

to acquire the FPS nanosheets (NSs). The synthesis details can be found in the experimental section. As shown in **Figure 1a**, the X-Ray diffraction (XRD) pattern of FPS NSs is attributed to the monoclinic structured Fe₂P₂S₆ (JCPDS #33-0672). The side- and top-view atomic structures of monoclinic FePS₃ are displayed in **Figure 1b** and **Figure S1**, Supporting Information, respectively. **Figure S1**, Supporting Information, indicates that in a typical unit cell, one Fe atom is connected to six neighboring S atoms; while the P atom is connected to one P atom and three S atoms. The side-view atomic structure of monoclinic FPS (**Figure 1b**) indicates the layered structure, confirming the feasibility of exfoliating bulk FPS into 2D FPS NSs. The as-synthesized FPS NSs were characterized by transmission electron microscopy (TEM), energy-dispersive X-ray spectroscopy (EDX), high-angle annular dark-field scanning transmission electron microscopy (HAADF-STEM), elemental mapping and atomic force microscopy (AFM). The TEM image of the FPS NSs in **Figure 1c** confirms the sheet-like structure of FPS NSs with lateral sizes of ≈320–380 nm. The EDX spectrum (**Figure 1d**) suggests the existence of Fe, P, and S elements. And the HAADF-STEM image and the corresponding elemental mapping images of Fe, P, and S (**Figure 1e**) together confirm the successful synthesis of FPS NSs. Furthermore, the AFM image of the FPS NSs (**Figure 1f**) and the corresponding height profiles (**Figure 1g**) show the FPS NS with a thickness of ≈20 nm, further supporting the successful fabrication of FPS NSs through the sonication treatment. In addition, to acquire FPS thin nanosheets (TNSs), the exfoliated FPS ethanol suspension was centrifugated at 7000 RPM instead of 3000 RPM. A detailed synthesis approach can be found in the Experimental section. As displayed in **Figure S2a,b**, Supporting Information, the obtained FPS TNS possesses a thickness of ≈5 nm, much thinner than that of FPS NSs (≈20 nm).

Then, we anchored the TiO₂ nanoparticles (NPs) on the FPS NSs utilizing a facile physical grinding approach. In detail, 0.05 g TiO₂ NPs were coupled with 1, 2, 5, and 10 mL of FPS NSs ethanol suspension, respectively. The as-synthesized samples were annotated as TF1, TF2, TF5, and TF10, respectively, and TiO₂ NPs alone were annotated as TF0. Based on the inductively coupled plasma-atomic emission spectroscopy (ICP-AES) result on the concentration of the FPS NSs ethanol solution (≈42.3 μg mL⁻¹), the contents of FPS NSs in TF5 and TF10 are estimated to be ≈0.42 and 0.84 wt%, respectively. Thus, due to the low content of FPS (≈0.42 wt%) in TF5, TEM, high-resolution (HR)TEM, EDX, elemental mapping, and AFM-Kelvin probe force microscopy (KPFM) were conducted on TF10 to investigate the physicochemical characteristics of TiO₂/FPS heterojunction. The XRD patterns of all the above samples are shown in **Figure 2a**. Both rutile-structured TiO₂ and anatase-structured TiO₂ can be observed in **Figure 2a**. No apparent diffraction peaks of FPS were observed, possibly owing to the low content of FPS in the combined samples. Raman spectroscopy was also conducted to acquire the structure information of TF0 and TF5. The Raman spectra for TF0 and TF5 are shown in **Figure S3**, Supporting Information. The peaks around 144, 200, 396, 516, and 635 cm⁻¹ could be assigned to the characteristic Raman modes of anatase TiO₂. No apparent difference in these peaks is observed for TF5 in comparison to those of TF0, suggesting the introduction of FPS does not impact the

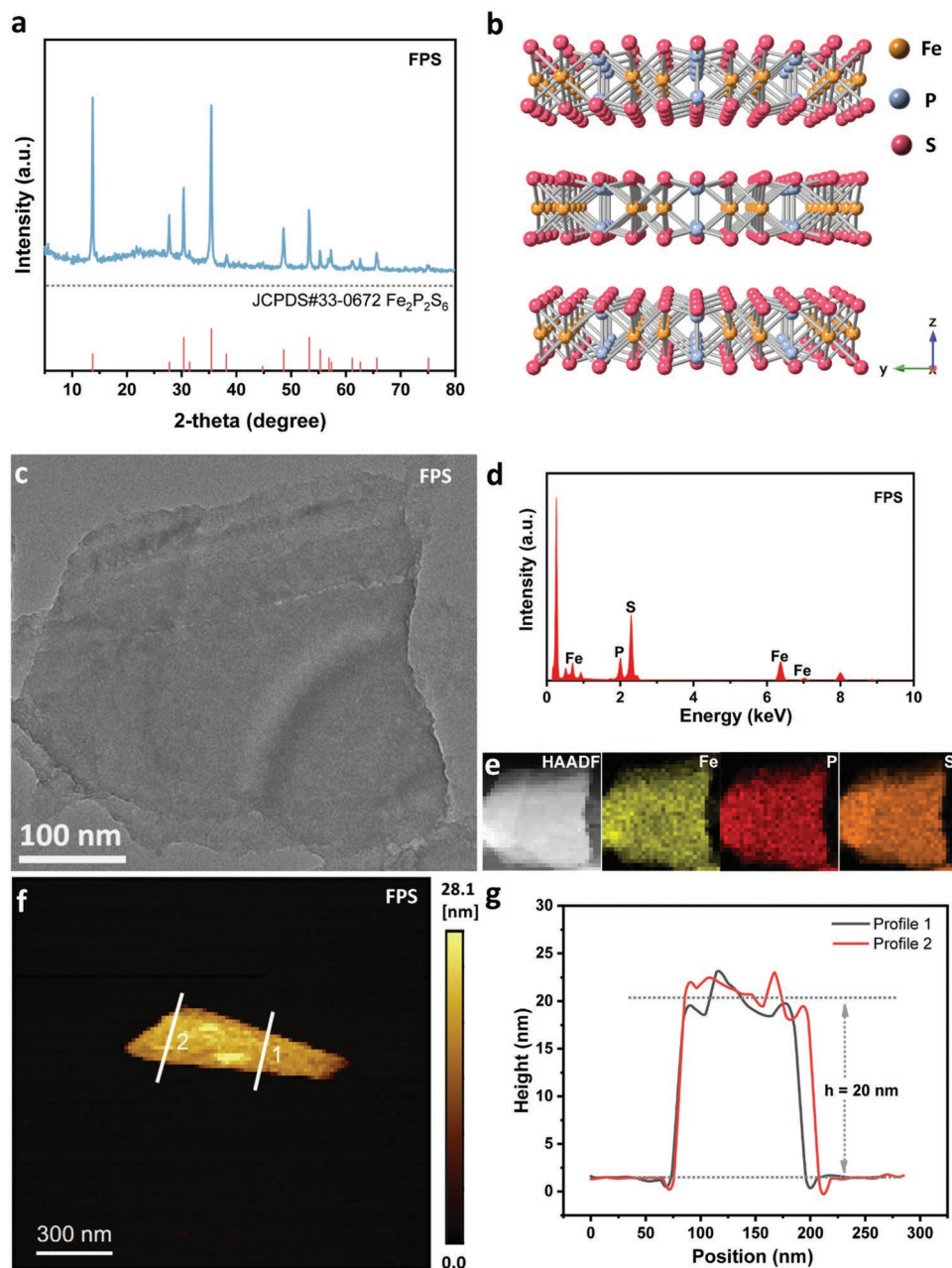


Figure 1. a) XRD pattern of FPS NSs. b) Side-view atomic structure of monoclinic FPS along [100] direction. c) TEM image of FPS NSs. d) EDX spectrum of FPS NSs. e) HAADF-STEM image and elemental mapping images of different elements in FPS NSs. f) AFM image and g) corresponding profiles of FPS NSs.

structure of TiO_2 . Synchrotron-based X-ray absorption near edge structure (XANES) spectra of Ti L edge for TF5 and TF10 are displayed in Figure S4, Supporting Information. Furthermore, the TEM image of TF10 is displayed in Figure 2b, which shows that the TiO_2 NPs are well dispersed on the FPS NSs. The 0.24 and 0.35 nm lattice spacings in the HRTEM image of TF10 (Figure 2c) are ascribed to the Anatase TiO_2 (103) and (101) facets, respectively. The EDX spectrum of TF10 (Figure 2d) confirms the existence of Ti, O, Fe, P, and S elements, corroborating the combination of TiO_2 NPs and FPS NSs in TF10. Furthermore, the HAADF-STEM image of TF10 and the element

distribution mapping of Ti, O, Fe, P, and S (Figure 2e) further support the intimate combination of TiO_2 NPs with FPS NSs. All the above results corroborate the successful anchoring of TiO_2 NPs on the FPS surface.

2.2. Photocatalytic H_2 Evolution Rate

To evaluate the performance of photocatalytic hydrogen (H_2) evolution reaction (pHER), all tests for the synthesized photocatalysts were measured in 10 vol% ethanol aqueous solution

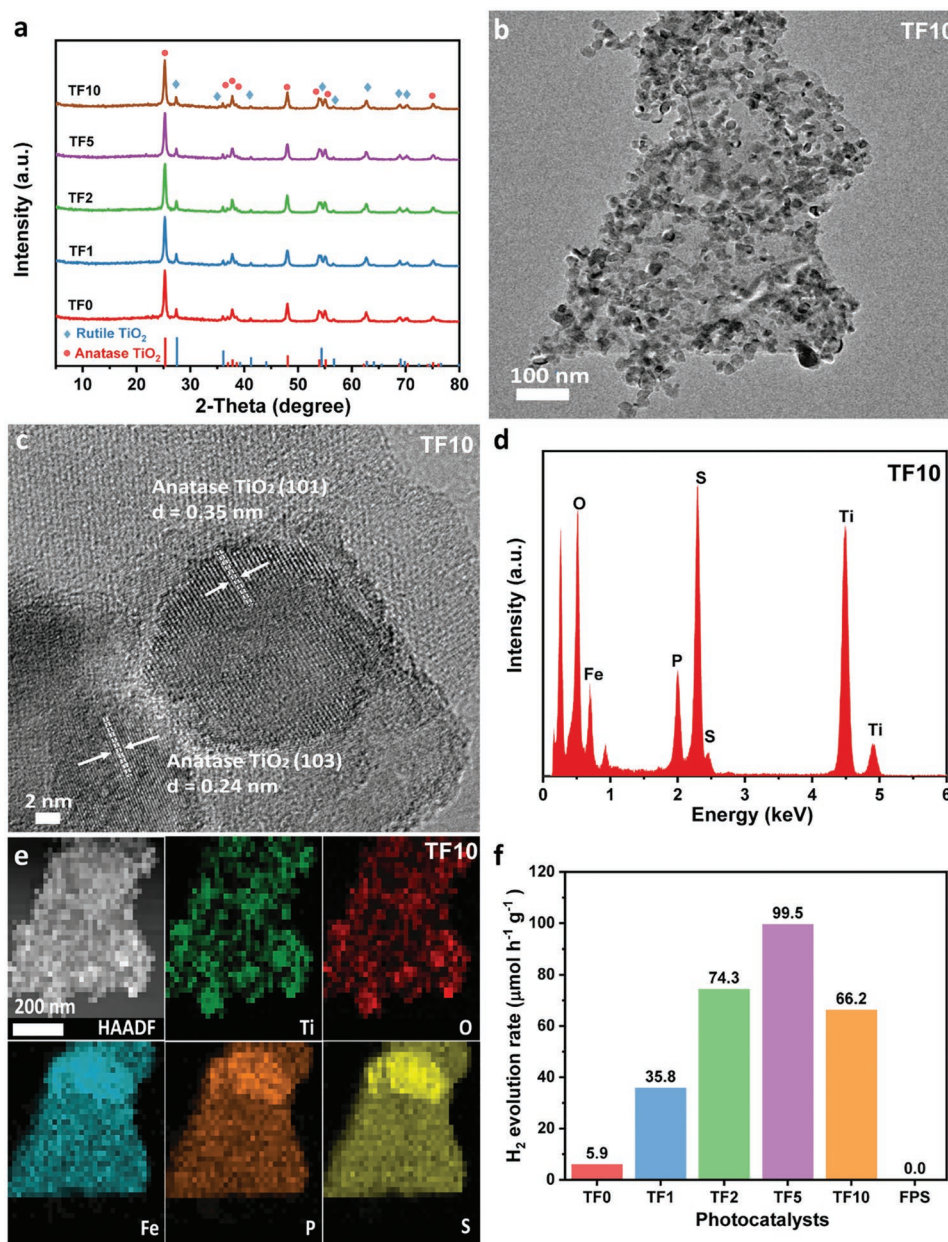


Figure 2. a) XRD patterns of TF0, TF1, TF2, TF5, and TF10. b) TEM, c) HRTEM images, and d) EDX spectrum of TF10. e) HAADF-STEM image and corresponding elemental mapping images of TF10. f) Photocatalytic H₂-evolution rates of TF0, TF1, TF2, TF5, TF10, and FPS in 10 vol% ethanol aqueous solution with xenon light illumination.

with xenon light irradiation. The pHER rate of pure TiO₂ (TF0) displayed in Figure 2f is about 5.9 μmol h⁻¹ g⁻¹, while no H₂ was generated if bare FPS was used as the photocatalyst. As for the TF_x ($x = 1, 2, 5, \text{ and } 10$) composites, their pHER rates were improved by the introduction of FPS NSs. Compared with the rate of TiO₂, the rates of TF1 and TF2 are raised to 35.8 and 74.3 μmol h⁻¹ g⁻¹, respectively. Strikingly, the rate of TF5 reaches its peak at 99.5 μmol h⁻¹ g⁻¹, surpassing the counterpart of TF0 by ≈1686%. Thus, TF5 exhibits an excellent activity compared with the other reported TiO₂-based photocatalysts (Table S2, Supporting Information). But further increasing the content of FPS does not arouse further activity enhance-

ment, since TF10 only shows a rate of 66.2 μmol h⁻¹ g⁻¹. This possibly results from the blockage of TiO₂ reactive sites and the weakening of the light-harvesting ability of TiO₂ due to excessive FPS NSs. Furthermore, we have tested the stability of TF5 on photocatalytic H₂-evolution for 9 h, with every 3 h as a cycle. As shown in Figure S5, Supporting Information, the H₂-evolution amount of TF5 on cycle 3 (268.6 μmol g⁻¹) accounts for ≈59.8% of that on cycle 1 (449.5 μmol g⁻¹). This result suggests acceptable stability of TF5. Then, we studied TF5 after the 9-h reaction (TF5-A) using high-angle annular dark field-scanning transmission electron microscopy (HAADF-STEM), EDX and elemental mapping. Figure S6a,

Supporting Information, shows the HAADF-STEM image of TF5-A, suggesting that TiO₂ NPs are still combined with FPS NSs after the 9-h reaction. The high-resolution HAADF-STEM image of TF5-A (Figure S6b, Supporting Information) shows the lattice spacing value of 0.32 nm, ascribed to the (002) facet of monoclinic FPS. Nevertheless, further observation in Figure S6c, Supporting Information, indicates the existence of some amorphous structures on the surface of FPS NSs. This is ascribed to the photo-corrosion and chemical corrosion of the FPS NSs that occurred during the 9-h reaction. The EDX spectrum of TF5-A (Figure S6d, Supporting Information) indicates the existence of Ti, O, Fe, P, and S elements, in agreement with the chemical composition of TF5 before reaction. Furthermore, the HAADF-STEM (Figure S7a, Supporting Information) and corresponding elemental mapping images (Figure S7b–f, Supporting Information) further confirm the combination of TiO₂ NPs with FPS NSs in TF5-A. All the above results reveal the acceptable stability of TF5. Additionally, we have also found that in each cycle, the first-hour rate is always lower than the second-hour or third-hour rate (Figure S5, Supporting Information). This is possibly due to the elevated temperature of the reaction system in the second and third hours compared to that in the first hour, which boosts the photocatalytic H₂ evolution reaction.^[50–53] Furthermore, we have also synthesized FPS TNS with a much thinner thickness of ≈5 nm (Figure S2a,b, Supporting Information). The concentration of FPS TNSs ethanol solution is determined to be ≈17.0 μg mL⁻¹ using ICP-AES. To keep the same amount of FPS in TF5, we used 12.5 mL ethanol

solution containing FPS TNSs to couple with 50 mg TiO₂ to synthesize TiO₂/FPS TNSs heterojunction, which is annotated as TF12.5-7000R. A detailed synthesis route can be found in the experimental section. The photocatalytic H₂-evolution rate on TF12.5-7000R was tested under the same conditions as that for TF5. As shown in Figure S8, Supporting Information, TF12.5-7000R exhibits the lower photocatalytic H₂-evolution activity (18.2 μmol h⁻¹ g⁻¹) compared to that of TF5 (99.5 μmol h⁻¹ g⁻¹). Nevertheless, this activity (18.2 μmol h⁻¹ g⁻¹) is still higher than that of TF0 (5.9 μmol h⁻¹ g⁻¹).

2.3. Charge Carrier Separation and Transfer

Since the separation/transfer of charge carriers serves a key role in the overall photocatalytic reaction, a range of cutting-edge characterizations were conducted to explore the photo-generated electron-hole dissociation and transport. First, steady-state photoluminescence (PL) spectroscopy and time-resolved photoluminescence (TRPL) were used to investigate the separation/transfer of charge carriers. Both TF0 and TF5 show two distinct peaks around 408 and 467 nm in Figure 3a, which are equal to 3.04 and 2.66 eV, respectively. The emission peak around ≈408 nm is attributed to the interband PL phenomenon. And the PL peak at ≈468 nm could be attributed to the band edge-free excitons. Anchoring of TiO₂ NPs on FPS NSs reduces the PL intensities of TiO₂, indicating that the charge recombination rate in TF5 is reduced, in contrast

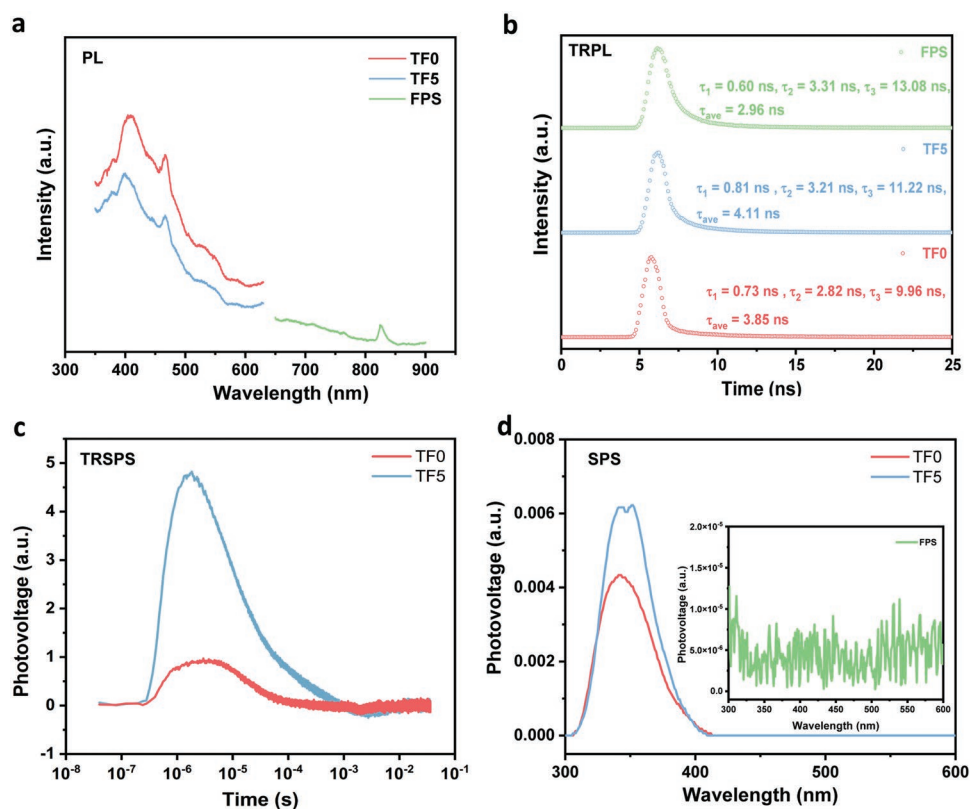


Figure 3. a) Steady-state PL spectra and b) TRPL spectra of TF0, TF5, and FPS. c) TRSPS spectra of TF0 and TF5. d) Steady-state SPS spectra of TF0, TF5, and FPS (inset).

to that in TF0. Additionally, the steady-state PL spectrum of FPS exhibits a PL peak at 826 nm, ascribed to the interband PL phenomenon of FPS.^[54] Furthermore, insights into the charge carrier lifetimes in TF0, TF5, and FPS can be acquired in the TRPL spectra (Figure 3b). As can be seen in Figure 3b and Table S3, Supporting Information, the fitted and average charge carrier lifetimes [$\tau_1 = 0.81$ ns (32.5%), $\tau_2 = 3.21$ ns (46.5%), $\tau_3 = 11.22$ ns (21.0%), and $\tau_{\text{ave}} = 4.11$ ns] of TF5 are obviously raised in contrast to those of TF0 [$\tau_1 = 0.73$ ns (30.2%), $\tau_2 = 2.82$ ns (46.5%), $\tau_3 = 9.96$ ns (23.3%), and $\tau_{\text{ave}} = 3.85$ ns]. The extended lifetime of the charge carriers in TF5 indicates a better dissociation of photogenerated electrons/holes than that in TiO₂ (TF0). In addition, Figure 3b and Table S3, Supporting Information, show the TRPL spectrum and fitted/average charge carrier lifetime [$\tau_1 = 0.60$ ns (58.6%), $\tau_2 = 3.31$ ns (28.7%), $\tau_3 = 13.08$ ns (12.7%), and $\tau_{\text{ave}} = 2.96$ ns] of FPS NSs. The reduced average charge carrier lifetime ($\tau_{\text{ave}} = 2.96$ ns) compared to those of TF0 ($\tau_{\text{ave}} = 3.85$ ns) and TF5 ($\tau_{\text{ave}} = 4.11$ ns) implies much easier recombination of charge carriers in FPS. These results are consistent with the negligible photocatalytic activity of FPS (0.0 $\mu\text{mol h}^{-1} \text{g}^{-1}$) compared to those of TF0 (5.9 $\mu\text{mol h}^{-1} \text{g}^{-1}$) and TF5 (99.5 $\mu\text{mol h}^{-1} \text{g}^{-1}$). Furthermore, time-resolved surface photovoltage spectroscopy (TRSPS) and steady-state surface photovoltage spectroscopy (SPS) were performed to reveal the surface charge carrier separation/transfer in TF5. As displayed in Figure 3c, both TF0 and TF5 show positive surface photovoltage signals, indicating that the photoinduced holes are accumulated on the surface after the light excitation. Furthermore, TF5 displays a much higher positive surface photovoltage signal than TF0, indicating that the anchoring of TiO₂ NPs on FPS NSs could greatly boost the accumulation of photogenerated holes on the surface. Considering that TiO₂ accounts for most of TF5, it can be inferred that the combination with FPS NSs advances dissociating electron-hole pairs in TiO₂ NPs and accumulating photogenerated holes on the surface of TiO₂ NPs. The steady-state SPS results in Figure 3d further confirm the higher surface photovoltage signal of TF5 compared with that of TF0, in agreement with the TRSPS result (Figure 3c). Besides, the surface photovoltage signal can only be observed as the excitation light wavelength is below ≈ 410 nm, confirming that the positive surface photovoltage is due to the surface accumulation of photogenerated holes from TiO₂ rather than FPS NSs. As shown in Figure 3d inset, FPS shows a very low photovoltage value in the range of 300–600 nm, due to the rapid recombination of photo-induced electrons and holes in FPS with a narrow band gap of 1.54 eV. Furthermore, all the photovoltage values of TF0, TF5, and FPS are positive (Figure 3d). This is because the steady-state photovoltage intensities acquired in this work are only absolute values. This result further confirms the rapid recombination of photo-excited electrons and holes in FPS, consistent with the negligible photocatalytic activity of FPS (Figure 2f). To reveal the efficiency of charge transfer, electrochemical impedance spectroscopy (EIS) was collected on the TF0, TF5, and FPS electrodes in 0.5 M Na₂SO₄ aqueous solution. The EIS Nyquist plots of TF0, TF5, and FPS are displayed in Figure S9, Supporting Information. TF5 exhibits a semicircle smaller than TF0 (TiO₂), indicating a reduced charge transfer resistance of TF5 compared with

that of TF0 (TiO₂). The inset flowchart (Figure S9, Supporting Information) exhibits the simulated equivalent circuit. Based on this simulation, the charge transfer resistance (R_{ct}) of TiO₂ is 6454 Ω , while that of TF5 is 5378 Ω . Furthermore, as shown in Figure S9, Supporting Information, the EIS Nyquist plot of FPS exhibits the smallest semicircle compared to those of TF0 and TF5, with the lowest charge transfer resistance ($R_{\text{ct}} = 1527$ Ω). These results reveal that the introduction of FPS NSs could decrease the charge transfer resistance of TiO₂ NPs, also supporting the better charge separation/transfer efficiency in TF5 compared with that of TF0. The above results indicate the greatly improved efficiency of charge separation/transfer after the coupling of TiO₂ NPs and FPS NSs in the TiO₂/FPS heterojunction. Hence, a variety of characterizations, such as in situ AFM-KPFM and in situ X-ray photoelectron spectroscopy (XPS), and theoretical computations were adopted to explore the reason. As shown in Figure 4a, the aggregation of TiO₂ NPs can be observed in the AFM image of TF10. Figure 4b,c shows the corresponding KPFM images of TF10 in darkness and with 365-nm UV light illumination, respectively. Accordingly, the surface potential profiles of TF10 in darkness and with 365-nm light irradiation are displayed in Figure 4d. It can be observed in Figure 4d that the surface potential at A1 is raised by 124 mV. The surface potentials across the line are all raised with the 365-nm light illumination compared to that in darkness. These results suggest that the photogenerated holes accumulate on the surface of TiO₂ NPs in TF10 with light excitation.

Furthermore, both ex situ and in situ XPS measurements were also conducted. Since the XPS technique cannot detect any Fe, P, and S signal in TF5 or TF10 due to the low contents of FPS in them, the amount of FPS NSs solution was increased to 50 mL for synthesizing TF50. The synthesis details are shown in the experimental section. As displayed in Figure 5a,b, the high-resolution XPS spectra of Ti 2p and O 1s for TF50 show the left shift of the Ti 2p and O 1s peaks toward the low binding energy direction, compared to those of TF0 (TiO₂). Besides, the high-resolution XPS spectra of Fe 2p_{3/2} (Figure 5c), P 2p (Figure S10a, Supporting Information), and S 2p (Figure S10b, Supporting Information) for TF50 exhibit the right shift toward the high binding energy direction, in contrast with those for FPS. These results support the transfer of electrons from FPS NSs to TiO₂ NPs after the combination in TF50. This also indicates the existence of a space charge region at the interface between TiO₂ and FPS in TF50, accompanied by the built-in electric field pointing from FPS to TiO₂ in this region in TF50. Furthermore, this also suggests the upward band bending of FPS and downward band bending of TiO₂ at the interface of FPS/TiO₂ heterojunction. Additionally, with light excitation, the O 1s peak of TF50 shifts toward higher binding energy positions, compared with that of TF50 without light excitation (Figure 5b). This result suggests that photogenerated holes are accumulated on the surface of TiO₂ NPs in TF50 after light excitation, agreeing with the TRSPS results (Figure 3c) and AFM-KPFM results (Figure 4d). Furthermore, the high-resolution XPS spectra of Fe 2p_{3/2} (Figure 5c), P 2p (Figure S10a, Supporting Information), and S 2p (Figure S10b, Supporting Information) for FPS shift to lower binding energy direction with light excitation, compared with those of FPS

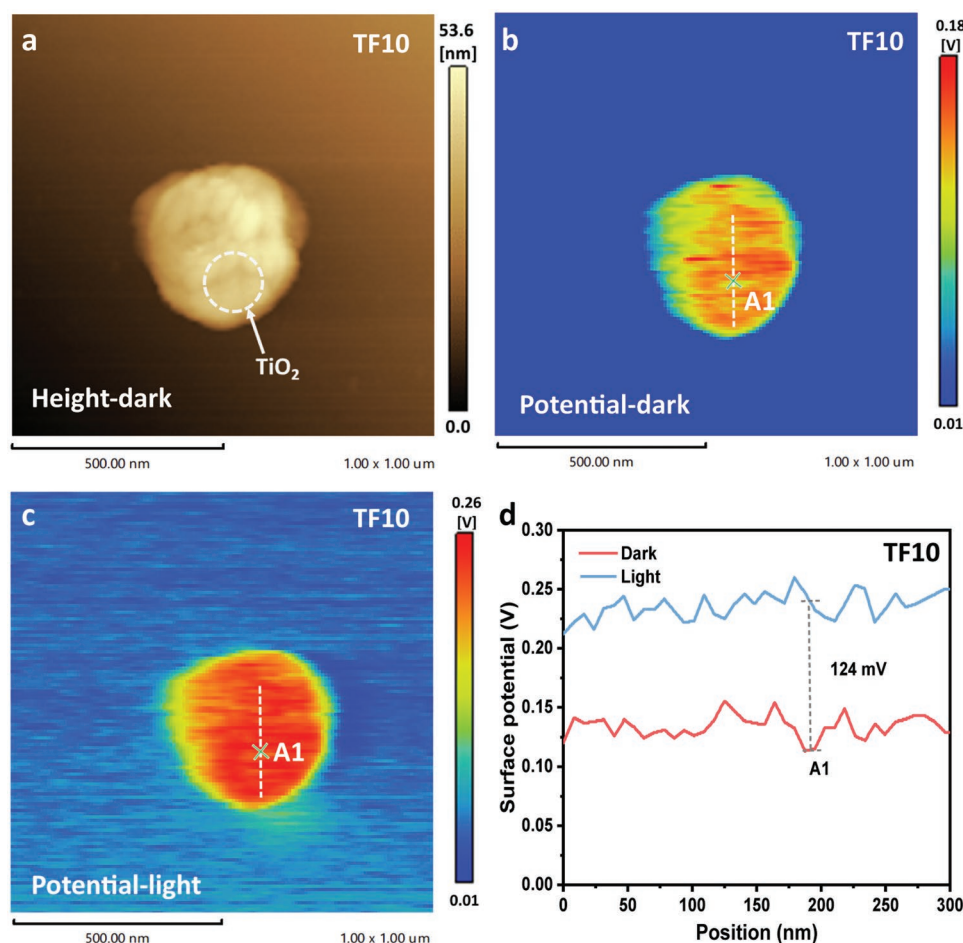


Figure 4. a) AFM and b) KPFM images of TF10 in darkness. c) KPFM image of TF10 with 365-nm UV light illumination. d) The corresponding surface potential profiles of TF10 in the dark and with 365-nm UV light illumination.

without light excitation. These suggest the accumulation of photogenerated electrons on the surface of FPS NSs in TF50 with light illumination.

In addition, the synchrotron-based XANES test was performed to explore the Fe K edge for TF5 and TF10. As shown in Figure S11, Supporting Information, the Fe K edge can be observed for both TF5 and TF10, confirming the existence of the Fe element in these two samples. Furthermore, the contact potential differences (CPDs) for FPS NSs and TiO₂ (TF0) in dark are shown in Figure S12, Supporting Information. And the work functions of FPS NSs and TiO₂ (TF0) are calculated to be 4.38 and 4.49 eV (Table S4, Supporting Information), respectively. This also supports the electron transport from FPS NSs to TF0 (TiO₂) after the contact in TF50, in agreement with the XPS spectra in Figure 5a,b. Furthermore, the differential charge density map of TiO₂ and FPS also bolsters the electron accumulation on TiO₂ at the interface of TiO₂/FPS (Figure 5d). Thus, all the above experimental and theoretical results support the extraction of electrons from FPS to TiO₂ after their contact in the TiO₂/FPS system. This confirms the intimate electronic coupling between TiO₂ and FPS in TiO₂/FPS system, and supports the existence of a built-in electric field and band bending at the interface between TiO₂ and FPS in TiO₂/FPS heterojunction.

2.4. Light Absorption and Surface Redox Reactions

In addition to the charge separation and migration, light absorption and redox reactions on the surface of the TiO₂/FPS system are also studied. All these samples were explored by ultraviolet-visible diffuse reflectance spectroscopy (UV-Vis DRS). The UV-Vis DRS spectra of all the samples (Figure 6a) exhibit an absorption edge around 387 nm, attributed to the absorption edge of TiO₂ with a bandgap energy of ≈ 3.20 eV. Compared to the UV-Vis DRS spectrum of TF0, all the TiO₂/FPS samples (TF1, TF2, TF5, and TF10) show an increased absorption ranging from ≈ 400 – 1000 nm, attributed to the absorption by FPS NSs. This confirms the intimate electronic interaction between FPS and TiO₂, which boosts the separation/transfer of photoinduced electrons and holes. This is confirmed by the long absorption edge of FPS NSs (804 nm; Figure 6b) that has a narrow bandgap (1.54 eV).

The surface redox reactions on the TiO₂/FPS system are closely related to the surface area and reactive sites. The nitrogen (N₂) adsorption-desorption isotherms for TF0 (TiO₂) and TF5 are shown in Figure 6c. The apparent shift up of sorption isotherm for TF5 is observed in the range of ≈ 0.8 – 1.0 of the relative pressure, suggesting that the

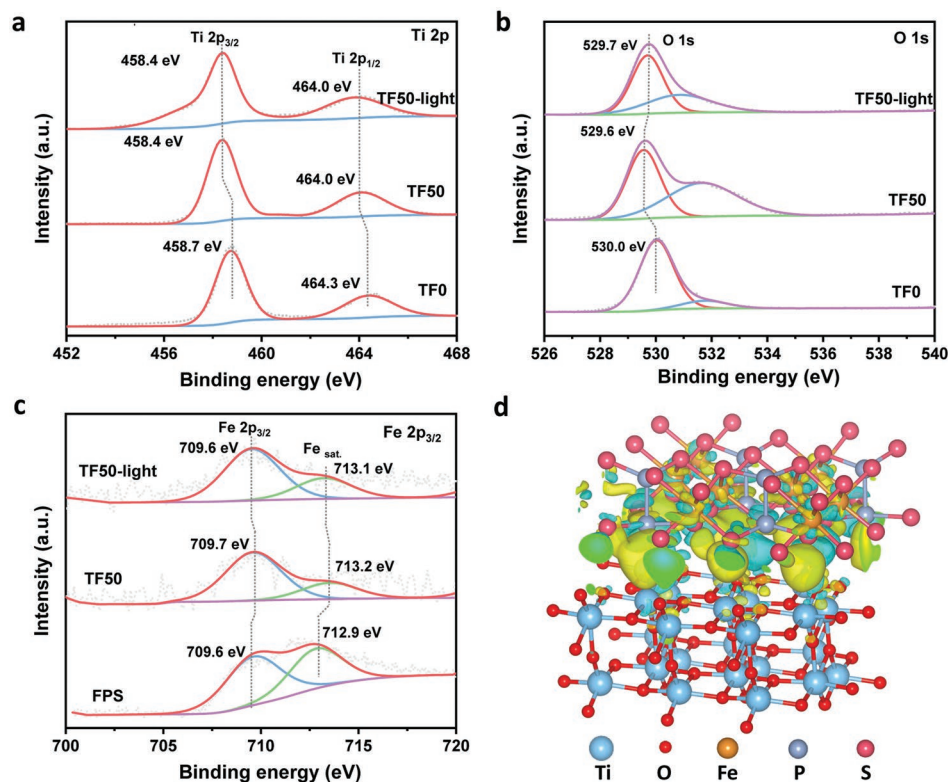


Figure 5. High-resolution XPS spectra of a) Ti 2p and b) O 1s for TF0 (TiO₂) without light illumination and TF50 without/with light illumination. c) High-resolution XPS spectra of Fe 2p_{3/2} for FPS NSs without light illumination and TF50 without/with light illumination. d) Side-view differential charge density map of TiO₂ (101) facet/FPS (001) facet with an iso-surface of $2.7 \times 10^{-4} \text{ e} \text{ \AA}^{-3}$. The charge is shown as the yellow region; while the charge depletion is shown as the cyan region.

introduction of FPS NSs would increase the macropores due to the aggregation of large-sized FPS NSs. However, the Brunauer–Emmett–Teller surface area (S_{BET}) for TF5 is slightly reduced to $46 \text{ m}^2 \text{ g}^{-1}$, slightly lower than the S_{BET} of TF0 ($49 \text{ m}^2 \text{ g}^{-1}$; Table S5, Supporting Information). The corresponding pore size distribution curves and parameters are displayed in Figure 6d and Table S5, Supporting Information, respectively. The N₂ sorption isotherm and corresponding pore size distribution curve of FPS NSs are also displayed. Furthermore, Table S5, Supporting Information indicates the much lower S_{BET} of FPS ($8 \text{ m}^2 \text{ g}^{-1}$) compared to that of TiO₂ (TF0; $49 \text{ m}^2 \text{ g}^{-1}$). This agrees with the much lower quantity adsorbed values of FPS than those of TiO₂ (TF0; Figure 6c). These results also support the reduced S_{BET} of TF5 ($46 \text{ m}^2 \text{ g}^{-1}$), in contrast with that of TF0. To investigate the intrinsic H₂ evolution reaction (HER) activities of TF0 and TF5, linear sweep voltammetry test was further conducted. As displayed in Figure S13, Supporting Information, FPS NSs show the best HER activity with the lowest potential to overcome at the current density of -0.5 mA cm^{-2} , while TF0 (TiO₂) shows the lowest HER activity. The HER overpotential of TF5 is reduced compared to that of TF0 at the same current density of -0.5 mA cm^{-2} . This result indicates that the addition of FPS NSs with active sites in TF5 could raise the HER activity and the proton reduction occurs on FPS in this TiO₂/FPS junction.

2.5. Reaction Mechanism Based on S-Scheme Heterojunction

The above experimental and theoretical calculation results confirm the construction of heterojunction between TiO₂ and FPS in the TiO₂/FPS system. To reveal the details of this heterojunction, further characterizations were carried out. First, the band structures of TiO₂ and FPS are calculated. As shown in Table S4, Supporting Information, the work functions of TiO₂ and FPS are 4.49 and 4.38 eV, respectively. Thus, the Fermi level (E_{F}) values of TiO₂ and FPS are 4.49 and 4.38 V versus (vs) vacuum level, equal to 0.05 and -0.06 V versus standard hydrogen electrode (SHE). Based on the valence band (VB) spectra of FPS and TiO₂ (Figure 7a), the VB edge potentials of FPS and TiO₂ are 0.56 and 2.84 V versus SHE. Since the bandgap energies of FPS and TiO₂ are 1.54 and 3.20 eV, the potentials for the conduction band (CB) edge of FPS and TiO₂ are -0.98 and -0.36 V versus SHE. The Mott–Schottky (MS) plots of FPS and TF5 at a frequency of 3000 Hz are shown in Figure S14, Supporting Information, and Figure 7b, respectively. Besides, the negative slope of the MS plot for FPS (Figure S14, Supporting Information) indicates that FPS is a p-type semiconductor. Furthermore, the MS plot of TF5 with positive slope (Region A) and negative slope (Region B) is observed in Figure 7b, suggesting the construction of an n-p junction in the TiO₂/FPS system. Hence, an S-scheme heterojunction mechanism based on the n-p semiconductor system is raised in this work. Before

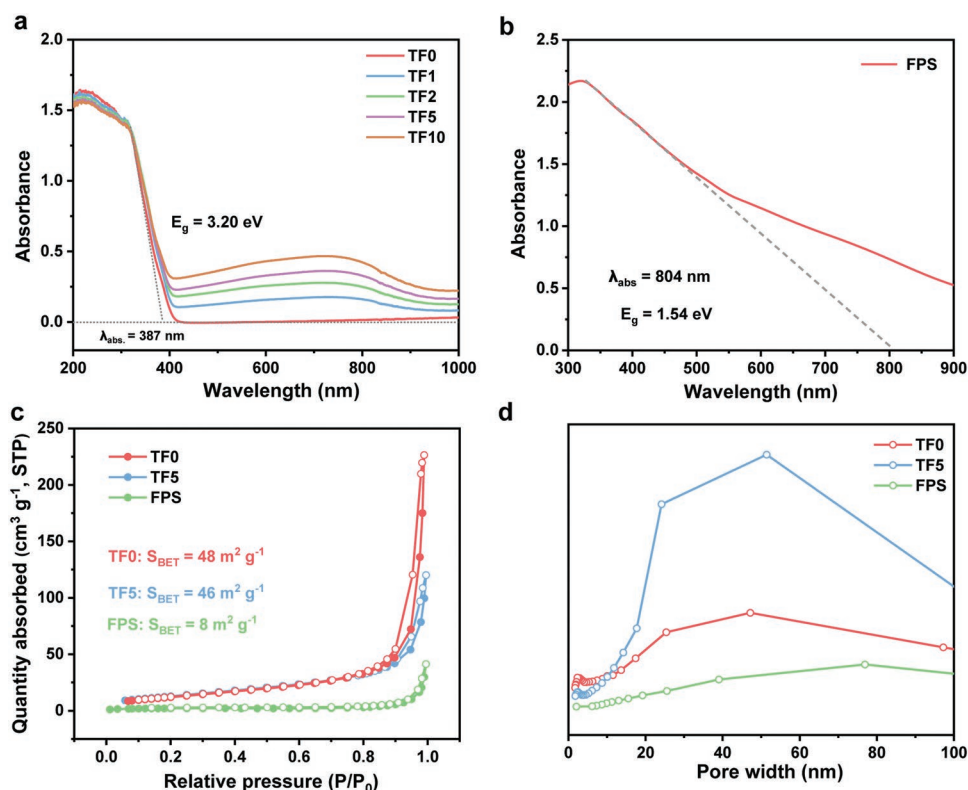


Figure 6. a) UV-vis DRS spectra of TF0, TF1, TF2, TF5, and TF10. b) UV-vis absorption spectrum of FPS NSs in ethanol solution. c) N_2 sorption isotherms and d) the corresponding pore size distribution curves of TF0, TF5, and FPS.

contact, the initial state of the band structure diagram of n-type TiO_2 and p-type FPS is shown in Figure 7c(i). Since the Fermi level potential (E_F) of FPS (-0.06 V vs SHE) is higher than that of TiO_2 (0.05 V vs SHE), the contact between TiO_2 and FPS leads to electron migration from FPS to TiO_2 , thus causing the upward curving of the CB and VB of FPS and the downward curving of the CB and VB of TiO_2 near the interface of FPS and TiO_2 to reach equilibrium and forming the built-in electric field as displayed in Figure 7c(ii). Upon light illumination, the electrons and holes are generated in both TiO_2 and FPS. Then, the photogenerated electrons of FPS are reserved in the CB of FPS and the photoinduced holes are retained in the VB of TiO_2 , owing to the strong built-in electric field near the interface of FPS and TiO_2 . Meanwhile, photogenerated electrons at the CB of TiO_2 are driven by the built-in electric field to recombine with the photogenerated holes in the VB of FPS. Hence, the stronger reduction ability derived from the photogenerated electrons in FPS and the stronger oxidation ability derived from the photogenerated holes are retained, respectively. And the high charge separation/transfer efficiency in TiO_2 /FPS system is achieved simultaneously. Also, photoexcited electrons at the CB of FPS could efficiently reduce the water molecules to generate H_2 gas due to the FPS surface active sites. And ethanol at TiO_2 can be easily oxidized by the strongly oxidative photogenerated holes in the VB to generate oxidized products. On basis of the reaction mechanism above, FPS functions as both the light absorber and catalyst to boost H_2 evolution. This is also corroborated by the reported works showing that FPS NSs alone possess photocatalytic H_2 evolution activities with xenon light illumination.^[27,28]

Since S-scheme heterojunction can reserve photo-induced electrons and holes with strong reduction/oxidation abilities, electron spin resonance (ESR) technique was adopted to further confirm the construction of S-scheme heterojunction. This is because the ESR technique can detect the reaction-yielded radicals (such as $\cdot OH$ and $\cdot O_2^-$) on TiO_2 , FPS, and TF5, and estimate the redox capabilities on these photocatalysts. As 5,5-dimethyl-1-pyrroline N-oxide (DMPO) was utilized as the spin-trapping agent, DMPO $\cdot OH$ and DMPO $\cdot O_2^-$ were detected after 5-min light illumination (Figure S15a,b, Supporting Information). The results in Figure S15a, Supporting Information, indicate the existence of highly-oxidative $\cdot OH$ in TF0 and TF5 aqueous solution after 5-min light illumination. Besides, Figure S15a, Supporting Information, also indicates the absence of $\cdot OH$ in the FPS aqueous solution. The above results are consistent with the fact that the VB edge of TiO_2 ($+2.84$ V vs SHE; Figure 7c) is more positive than the standard reduction potential of $E^0(\cdot OH/OH^-)$ ($+2.80$ V vs SHE); while the VB edge of FPS ($+0.56$ V vs SHE) is much less positive than that. Additionally, stronger signals of DMPO $\cdot OH$ for TF5 are observed in Figure S15a, Supporting Information, compared with those for TF0. This is due to the raised separation/transfer efficiency of photo-induced electrons/holes in TF5 S-scheme heterojunction, compared to that in TF0. Furthermore, Figure S15b, Supporting Information, indicates the existence of $\cdot O_2^-$ in TF0 and TF5 methanol solution after 5-min light illumination. This is because the CB edge of TiO_2 (-0.36 V vs SHE; Figure 7c) or that of FPS (-0.98 V vs SHE; Figure 7c) is more negative than the standard reduction potential

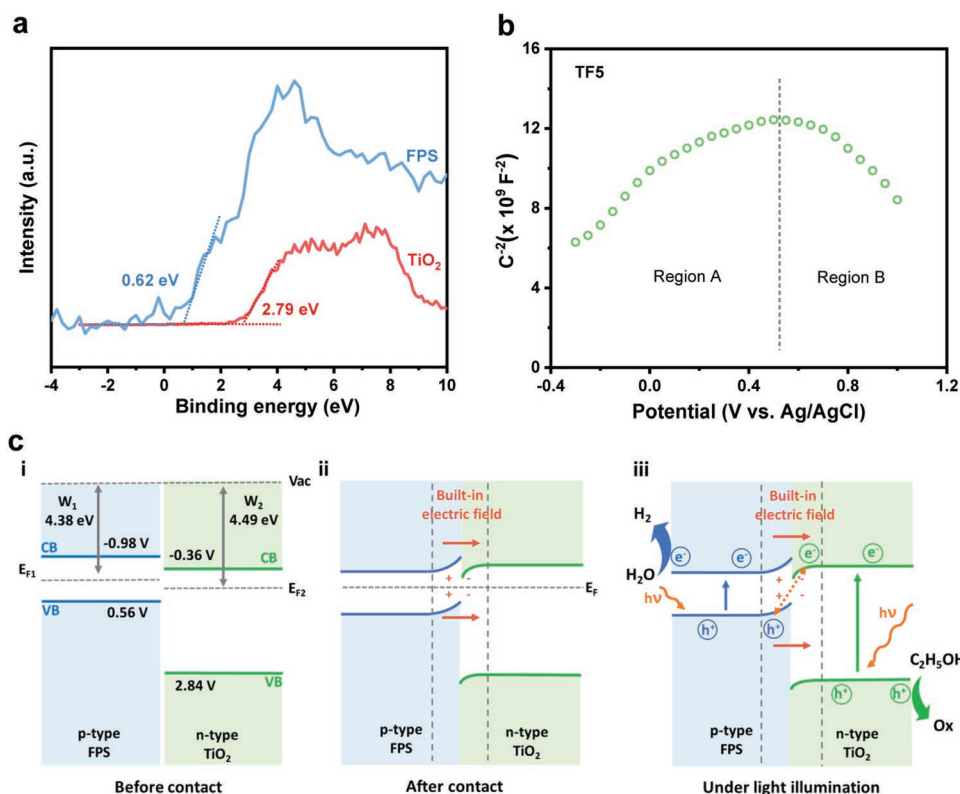


Figure 7. a) XPS VB spectra of TiO₂ and FPS. b) Mott-Schottky plot for TF5 acquired in 0.5 M Na₂SO₄ aqueous solution at the frequency of 3000 Hz. c) Reaction mechanism for photocatalytic H₂ evolution on S-scheme TiO₂/FPS heterojunction: i) before contact, ii) after contact, and iii) under light illumination.

of E⁰(O₂/•O₂⁻) (-0.33 V vs SHE). In contrast, negligible signals of DMPO•O₂⁻ are observed for FPS in methanol solution, due to the rapid recombination of photo-induced electrons and holes in FPS. In addition, stronger signals are found for TF5 than those of TF0, owing to the raised charge dissociation/transport efficiency in TF5. It should be noted that no ESR signal is observed in the blank experiments, indicating that the DMPO molecule has no paramagnetic response. Therefore, all the above results in Figure S15a,b, Supporting Information corroborate the successful construction of the S-scheme heterojunction in TF5.

3. Conclusions

In summary, the S-scheme TiO₂/FePS₃ heterojunction was successfully fabricated by the self-assembly of TiO₂ nanoparticles (NPs) and FePS₃ (FPS) nanosheets (NSs). The formation of TiO₂/FPS S-scheme heterojunction leads to establishing a strong internal electric field, which not only retains the stronger redox capabilities of the photoexcited electrons and holes, but also achieves higher electron-hole separation efficiency via recombining the photogenerated electrons and holes with weaker redox abilities. Additionally, the FPS NSs accommodate the reactive sites for the hydrogen (H₂) generation reaction. Therefore, greatly raised photocatalytic H₂ evolution activity was achieved over the TiO₂/FPS S-scheme heterojunction. These are supported by both theoretical calculations and cutting-edge characterization techniques, for example, synchrotron-based

X-ray absorption near edge structure (XANES), transient-state surface photovoltage spectroscopy/photoluminescence spectroscopy, in situ atomic force microscopy combined with Kelvin probe force microscopy (AFM-KPFM) and in situ X-ray photoelectron spectroscopy (XPS). This work not only demonstrates the great capacity of increasing photocatalytic activity by the construction of S-scheme heterojunction with a strong internal electric field, but also highlights the new way for the development of efficient, affordable, and durable high-activity photocatalysts with new 2D materials.

4. Experimental Section

All chemicals were used without further purification if not specified.

Synthesis of FPS Nanosheets: The bulk FPS was bought from a commercial supplier. First, 100 mg bulk FPS was ground into black powder for 0.5 h and added into 100 mL ethanol. The mixed suspension was then sonicated by a 600 W ultrasonic cell crusher (Ningbo Xinzhi Biotechnology Ltd. Co.) for 10 h. After centrifugation at 3000 RPM for 5 min, the supernatant was collected and centrifuged at 10000 RPM for another 5 min. Then the supernatant was disposed and the black precipitates were well dispersed in 100 mL ethanol and used as FPS NSs.

Synthesis of FPS Thin Nanosheets: FPS TNSs were synthesized using the same approach as synthesizing FPS NSs except that the exfoliated FPS ethanol suspension was first centrifuged at 7000 RPM instead of 3000 RPM for 5 min.

Synthesis of TiO₂/FPS: The TiO₂/FPS samples were synthesized by grinding at room temperature. Typically, 50 mg TiO₂ (P25, Degussa AG) was added into a certain amount ($x = 1, 2, 5, 10, \text{ and } 50 \text{ mL}$) of FPS

NSs suspension. The mixture was then ground for 0.5 h followed by 3-h natural drying, and the final products were collected and annotated as TFx.

Synthesis of TF12.5-7000R: TF12.5-7000R was synthesized by grinding 50 mg TiO₂ (P25, Degussa AG) with 12.5 mL FPS TNSs ethanol solution. The mixture was then grounded for 0.5 h followed by 3-h natural drying, and the final products were collected and annotated as TF12.5-7000R.

Evaluation of Photocatalytic H₂ Evolution Activity: Briefly, 20 mg photocatalyst TFx were added into a 100 mL sealed reactor containing 80 mL 10 vol% ethanol aqueous solution. The mixed solution was bubbled with nitrogen (N₂) for 0.5 h. A 350 W Xenon arc lamp ($\lambda > 350$ nm) was employed for light irradiation while the reactor was 10 cm away from the lamp. 0.4 mL evolved gas under light irradiation was extracted intermittently with a syringe and injected into the detector of the Shimadzu gas chromatograph (GC-14C). The amount of generated H₂ was calculated by analyzing the peak area of evolved H₂ and standard H₂.

Details about physicochemical characterization, electrochemical measurements and theoretical calculations are available in Supporting Information.

Supporting Information

Supporting Information is available from the Wiley Online Library or from the author.

Acknowledgements

The authors gratefully acknowledge the financial support from the Australian Research Council (ARC) through the Discovery Project programs (FL170100154, DE200100629, and DP220102596). B.X. thanks Prof. Liqiang Jing and Dr. Yang Qu from Heilongjiang University for their assistance with SPS and TRSPS measurement, and Dr. Zhongliao Wang from the Wuhan University of Technology for the assistance with computation. XANES measurement was conducted at the Australian Synchrotron (AS).

Open access publishing facilitated by The University of Adelaide, as part of the Wiley - The University of Adelaide agreement via the Council of Australian University Librarians.

Conflict of Interest

The authors declare no conflict of interest.

Data Availability Statement

The data that support the findings of this study are available from the corresponding author upon reasonable request.

Keywords

2D materials, in situ atomic force microscopy, in situ X-ray photoelectron spectroscopy, Kelvin probe force microscopy, photocatalytic hydrogen evolution, S-scheme heterojunctions

Received: April 28, 2022
Revised: September 25, 2022
Published online:

- [1] R. R. Hernandez, A. Armstrong, J. Burney, G. Ryan, K. Moore-O'Leary, I. Diédhiou, S. M. Grodsky, L. Saul-Gershenz, R. Davis, J. Macknick, D. Mulvaney, G. A. Heath, S. B. Easter, M. K. Hoffacker, M. F. Allen, D. M. Kammen, *Nat. Sustain.* **2019**, *2*, 560.
- [2] S. D. Tilley, *Adv. Energy Mater.* **2019**, *9*, 1802877.
- [3] J. Gong, C. Li, M. R. Wasielewski, *Chem. Soc. Rev.* **2019**, *48*, 1862.
- [4] O. A. Al-Shahri, F. B. Ismail, M. A. Hannan, M. S. H. Lipu, A. Q. Al-Shetwi, R. A. Begum, N. F. O. Al-Muhsen, E. Soujeri, *J. Cleaner Prod.* **2021**, *284*, 125465.
- [5] D. K. Dogutan, D. G. Nocera, *Acc. Chem. Res.* **2019**, *52*, 3143.
- [6] S. Ye, C. Ding, M. Liu, A. Wang, Q. Huang, C. Li, *Adv. Mater.* **2019**, *31*, 1902069.
- [7] T. Keijer, T. Bouwens, J. Hessels, J. N. H. Reek, *Chem. Sci.* **2021**, *12*, 50.
- [8] S. Chen, Y. Qi, C. Li, K. Domen, F. Zhang, *Joule* **2018**, *2*, 2260.
- [9] W. Zhong, D. Gao, H. Yu, J. Fan, J. Yu, *Chem. Eng. J.* **2021**, *419*, 129652.
- [10] S. Tang, Y. Xia, J. Fan, B. Cheng, J. Yu, W. Ho, *Chin. J. Catal.* **2021**, *42*, 743.
- [11] Q. Wang, K. Domen, *Chem. Rev.* **2020**, *120*, 919.
- [12] K. Takanahe, *ACS Catal.* **2017**, *7*, 8006.
- [13] B. Xia, Y. Zhang, B. Shi, J. Ran, K. Davey, S. Z. Qiao, *Small Methods* **2020**, *4*, 2000063.
- [14] J. Xiong, J. Di, J. Xia, W. Zhu, H. Li, *Adv. Funct. Mater.* **2018**, *28*, 1801983.
- [15] G. Guan, E. Ye, M. You, Z. Li, *Small* **2020**, *16*, 1907087.
- [16] Z. Xie, Y.-P. Peng, L. Yu, C. Xing, M. Qiu, J. Hu, H. Zhang, *Sol. RRL* **2020**, *4*, 1900400.
- [17] Y. Zhou, Z. Wang, L. Huang, S. Zaman, K. Lei, T. Yue, Z. a. Li, B. You, B. Y. Xia, *Adv. Energy Mater.* **2021**, *11*, 2003159.
- [18] D. Qin, Y. Zhou, W. Wang, C. Zhang, G. Zeng, D. Huang, L. Wang, H. Wang, Y. Yang, L. Lei, S. Chen, D. He, *J. Mater. Chem. A* **2020**, *8*, 19156.
- [19] R. Hu, G. Liao, Z. Huang, H. Qiao, H. Liu, Y. Shu, B. Wang, X. Qi, *J. Hazard. Mater.* **2021**, *405*, 124179.
- [20] Y. Xia, B. Cheng, J. Fan, J. Yu, G. Liu, *Sci. China Mater.* **2020**, *63*, 552.
- [21] B. Chen, D. Wang, J. Tan, Y. Liu, M. Jiao, B. Liu, N. Zhao, X. Zou, G. Zhou, H.-M. Cheng, *J. Am. Chem. Soc.* **2022**, *144*, 3106.
- [22] S. Ghosh, F. Kargar, A. Mohammadzadeh, S. Rumyantsev, A. A. Balandin, *Adv. Electron. Mater.* **2021**, *7*, 2100408.
- [23] C. R. S. Haines, M. J. Coak, A. R. Wildes, G. I. Lampronti, C. Liu, P. Nahai-Williamson, H. Hamidov, D. Daisenberger, S. S. Saxena, *Phys. Rev. Lett.* **2018**, *121*, 266801.
- [24] J. Xu, W. Li, Y. Hou, *Trends Chem.* **2020**, *2*, 163.
- [25] W. Zhu, W. Gan, Z. Muhammad, C. Wang, C. Wu, H. Liu, D. Liu, K. Zhang, Q. He, H. Jiang, X. Zheng, Z. Sun, S. Chen, L. Song, *Chem. Commun.* **2018**, *54*, 4481.
- [26] Z. Yu, J. Peng, Y. Liu, W. Liu, H. Liu, Y. Guo, *J. Mater. Chem. A* **2019**, *7*, 13928.
- [27] H. Wang, Z. Li, Y. Li, B. Yang, J. Chen, L. Lei, S. Wang, Y. Hou, *Nano Energy* **2021**, *81*, 105613.
- [28] Z. Cheng, T. A. Shifa, F. Wang, Y. Gao, P. He, K. Zhang, C. Jiang, Q. Liu, J. He, *Adv. Mater.* **2018**, *30*, 1707433.
- [29] J. Zhang, F. Feng, Y. Pu, X. a. Li, C. H. Lau, W. Huang, *ChemSusChem* **2019**, *12*, 2651.
- [30] P. Sen, R. K. Chouhan, *Electron. Struct.* **2020**, *2*, 025003.
- [31] R. Chen, F. Fan, T. Dittrich, C. Li, *Chem. Soc. Rev.* **2018**, *47*, 8238.
- [32] M. J. Shearer, M.-Y. Li, L.-J. Li, S. Jin, R. J. Hamers, *J. Phys. Chem. C* **2018**, *122*, 13564.
- [33] B. He, C. Bie, X. Fei, B. Cheng, J. Yu, W. Ho, A. A. Al-Ghamdi, S. Wageh, *Appl. Catal., B* **2021**, *288*, 119994.
- [34] J. Bian, Z. Zhang, J. Feng, M. Thangamuthu, F. Yang, L. Sun, Z. Li, Y. Qu, D. Tang, Z. Lin, F. Bai, J. Tang, L. Jing, *Angew. Chem., Int. Ed.* **2021**, *60*, 20906.
- [35] L. Zhang, J. Zhang, H. Yu, J. Yu, *Adv. Mater.* **2022**, *34*, 2107668.

- [36] C. Cheng, B. He, J. Fan, B. Cheng, S. Cao, J. Yu, *Adv. Mater.* **2021**, *33*, 2100317.
- [37] Q. Xu, S. Wageh, A. A. Al-Ghamdi, X. Li, *J. Mater. Sci. Technol.* **2022**, *124*, 171.
- [38] F. Y. Xu, K. Meng, S. Cao, C. H. Jiang, T. Chen, J. S. Xu, J. G. Yu, *ACS Catal.* **2022**, *12*, 164.
- [39] M. Sayed, B. Zhu, P. Kuang, X. Liu, B. Cheng, A. A. A. Ghamdi, S. Wageh, L. Zhang, J. Yu, *Adv. Sustainable Syst.* **2021**, *6*, 2100264.
- [40] S. Wageh, A. A. Al-Ghamdi, O. A. Al-Hartomy, M. F. Alotaibi, L. Wang, *Chin. J. Catal.* **2022**, *43*, 586.
- [41] X. Li, B. Kang, F. Dong, Z. Zhang, X. Luo, L. Han, J. Huang, Z. Feng, Z. Chen, J. Xu, B. Peng, Z. L. Wang, *Nano Energy* **2021**, *81*, 105671.
- [42] Q. Xu, L. Zhang, B. Cheng, J. Fan, J. Yu, *Chem* **2020**, *6*, 1543.
- [43] J. Fu, Q. Xu, J. Low, C. Jiang, J. Yu, *Appl. Catal., B* **2019**, *243*, 556.
- [44] L. Wang, B. Cheng, L. Zhang, J. Yu, *Small* **2021**, *17*, 2103447.
- [45] P. Xia, S. Cao, B. Zhu, M. Liu, M. Shi, J. Yu, Y. Zhang, *Angew. Chem., Int. Ed.* **2020**, *59*, 5218.
- [46] J. Li, Y. Long, Z. Hu, J. Niu, T. Xu, M. Yu, B. Li, X. Li, J. Zhou, Y. Liu, C. Wang, L. Shen, W. Guo, J. Yin, *Nat. Commun.* **2021**, *12*, 4998.
- [47] V. Donchev, *Mater. Res. Express* **2019**, *6*, 103001.
- [48] M. A. Melo, Z. Wu, B. A. Nail, A. T. De Denko, A. F. Nogueira, F. E. Osterloh, *Nano Lett.* **2018**, *18*, 805.
- [49] Z.-K. Xin, Y.-J. Gao, Y. Gao, H.-W. Song, J. Zhao, F. Fan, A.-D. Xia, X.-B. Li, C.-H. Tung, L.-Z. Wu, *Adv. Mater.* **2022**, *34*, 2106662.
- [50] Y. Li, Y.-K. Peng, L. Hu, J. Zheng, D. Prabhakaran, S. Wu, T. J. Puchler, M. Li, K.-Y. Wong, R. A. Taylor, S. C. E. Tsang, *Nat. Commun.* **2019**, *10*, 4421.
- [51] K. Wang, Z. Xing, D. Meng, S. Zhang, Z. Li, K. Pan, W. Zhou, *Appl. Catal. B* **2021**, *281*, 119482.
- [52] F. Meng, Y. Liu, J. Wang, X. Tan, H. Sun, S. Liu, S. Wang, *J. Colloid Interface Sci.* **2018**, *532*, 321.
- [53] S. Fang, Y. Liu, Z. Sun, J. Lang, C. Bao, Y. H. Hu, *Appl. Catal. B* **2020**, *278*, 119316.
- [54] J. Duan, P. Chava, M. Ghorbani-Asl, Y. Lu, D. Erb, L. Hu, A. Echresh, L. Rebohle, A. Erbe, A. V. Krashennnikov, M. Helm, Y.-J. Zeng, S. Zhou, S. Prucnal, *ACS Appl. Mater. Interfaces* **2022**, *14*, 11927.